remote sensing

Communication

Regularized CNN Feature Hierarchy for Hyperspectral Image Classification

Muhammad Ahmad [1,2,*], Manuel Mazzara [3] and Salvatore Distefano [2]

[1] Department of Computer Science, Chiniot-Faisalabad Campus, National University of Computer and Emerging Sciences, Islamabad, Chiniot 35400, Pakistan
[2] Dipartimento di Matematica e Informatica-MIFT, University of Messina, 98121 Messina, Italy; sdistefano@unime.it
[3] Institute of Software Development and Engineering, Innopolis University, 420500 Innopolis, Russia; m.mazzara@innopolis.ru
* Correspondence: mahmad00@gmail.com

Abstract: Convolutional Neural Networks (CNN) have been rigorously studied for Hyperspectral Image Classification (HSIC) and are known to be effective in exploiting joint spatial-spectral information with the expense of lower generalization performance and learning speed due to the hard labels and non-uniform distribution over labels. Therefore, this paper proposed an idea to enhance the generalization performance of CNN for HSIC using soft labels that are a weighted average of the hard labels and uniform distribution over ground labels. The proposed method helps to prevent CNN from becoming over-confident. We empirically show that, in improving generalization performance, regularization also improves model calibration, which significantly improves beam-search. Several publicly available Hyperspectral datasets are used to validate the experimental evaluation, which reveals improved performance as compared to the state-of-the-art models with overall 99.29%, 99.97%, and 100.0% accuracy for Indiana Pines, Pavia University, and Salinas dataset, respectively.

Keywords: beam-search; regularization; hybrid convolutional neural network (CNN); hyperspectral images classification (HSIC)

Citation: Ahmad, M.; Mazzara, M.; Distefano, S. Regularized CNN Feature Hierarchy for Hyperspectral Image Classification. *Remote Sens.* **2021**, *13*, 2275. https://doi.org/10.3390/rs13122275

Academic Editor: Bogdan Zagajewski

Received: 28 April 2021
Accepted: 7 June 2021
Published: 10 June 2021

1. Introduction

Hyperspectral Imaging (HSI) has been extensively utilized for many real-world applications [1]—for instance, crop monitoring [2], vegetation coverage [3], precision agriculture [4], land resources [5], oil spills [6], water quality [7], meat adulteration [8,9], adulteration in household products such as color adulteration in red chili [10,11], microbial spoilage, and shelf-life of bakery products [12].

Thus, HSI Classification (HSIC) has received remarkable attention and intensive research results have been reported in the past few decades [13]. According to the literature, HSIC can be categorized into spatial, spectral, and spatial-spectral feature methods [14]. The spectral feature can be labeled as a primitive characteristic of HSI also known as spectral curve or vector, whereas the spatial feature contains the relationship between the central pixel and its context, which significantly improves the performance [15].

In the last few years, deep learning, especially Convolutional Neural Networks (CNNs), has received widespread attention due to its ability to automatically learn non-linear features for classification, i.e., overcome the challenges of hand-crafted features for HSIC using traditional methods [16] such as Support Vector Machine (SVM), K-Nearest Neighbor (KNN), Random Forest, Ensemble Learning, Artificial Neural Network, and Extreme Learning Machine (ELM) [17,18]. Moreover, CNN can jointly investigate the spatial-spectral information and such models can be categorized into two groups, i.e., single and two-stream; more information regarding single or two-stream methods can be found in [19]. This work explicitly investigates a single-stream method similar to the works proposed by Ahmad et al. [20] (A Fast and Compact 3D CNN for HSIC), Xie et al. [21] (Hyperspectral Face Recognition-based on Sparse Spectral Attention Deep Neural Network), Liu et al. [22] (A semi-supervised CNN for HSIC), Hamida et al. [23] (3D Deep Learning Approach for Remote Sensing Image Classification), Lee et al. [24] (Contextual Deep CNN-based HSIC), Chen et al. [25] (Contextual Deep CNN-based HSIC), Li [26] (Spectral–Spatial Classification of HSI with 3D CNN), He et al. [27] (Multi-scale 3D Deep CNN Network for HSI), Zhao et al. [28] (Hybrid Depth-Separable Residual Networks for HSIC). Yang et al. [29] (Synergistic 2D/3D CNN for HSIC).

Irrespective of the single or two-stream methods, all deep learning frameworks discussed above are sensitive to the loss, which needs to be minimized [30]. Several classical works showed that the gradient descent to minimize cross-entropy performs better in terms of classification and has fast convergence; however, to some extent, this leads to the overfitting [31]. Several regularization techniques, such as dropout [32], L1, L2 [33], etc., have been used to overcome the overfitting issues together with several other exotic objectives performed exceptionally well compared to the standard cross-entropy [34]. Recently, a work [35] proposed a regularization technique that improves the accuracy significantly by computing cross-entropy with a weighted mixture of targets with uniform distribution instead of hard-coded targets.

Since then, regularization has been known to improve the classification performance of deep models [36]. However, the original idea was used to improve the classification performance of only the inception model on ImageNet data [35]. Despite this, various image classification models have used regularization [37,38]. Though the regularization technique is a widely used trick to improve the classification performance and to speed up the convergence process, it has not been much explored for HSIC, and, above all, regarding when and why regularization should work have not been explored very much.

Considering the aforementioned issues, this paper proposed a novel idea to enhance the generalization performance of CNN for HSIC using soft labels that are a weighted average of the hard labels and uniform distribution over target labels. The proposed method helps to prevent CNN from becoming over-confident. We empirically show that, in improving generalization performance, regularization also improves model calibration, which significantly improves beam-search. Several publicly available Hyperspectral datasets are used to validate the experimental evaluation, which reveals improved generalization performance, statistical significance, and computational complexity as compared to the state-of-the-art 2D/3D CNN models.

2. Problem Formulation

Let us assume that the Hyperspectral data can be represented as $R^{(M \times N) \times B^*} = [r_1, r_2, r_3, \ldots, r_S]^T$, where B^* is the total number of bands. $(M \times N)$ are the samples per band belonging to Y classes and $r_i = [r_{1,i},\ r_{2,i},\ r_{3,i},\ \ldots, r_{B^*,i}]^T$ is the ith sample in the Hyperspectral Data. Suppose $(r_i, y_i) \in (\mathcal{R}^{M \times N \times B^*}, \mathcal{R}^Y)$, where y_i is the class label of the ith sample. For HSI classification with Y candidate labels, for example, lets assume $(r_i, y_i) \in (\mathcal{R}^{M \times N \times B^*}, \mathcal{R}^Y)$, where y_i is the class label of the r_i sample belonging to the training set and the ground truth distribution p over labels $p(y|r_i)$ and $\sum_{y=1}^{Y} p(y|r_i) = 1$. One can have a model with parameters θ that predicts the predicted label distribution as $q_\theta(y|r_i)$ and, of course, $\sum_{y=1}^{Y} q_\theta(y|r_i) = 1$. Thus, the cross entropy in this particular case would be $H_i(p, q_\theta) = \sum_{y=1}^{Y} p(y|r_i)\ log\ q_\theta(y|r_i)$.

If one have $M \times N$ instance in the training set, then the loss function would be $L = H_i(p, q_\theta)$ which can further modify as $L = -\sum_{i=1}^{M \times N} \sum_{j=1}^{Y} p(y|r_i)\ log\ 1_\theta(y|r_i)$. However, in nature, the $p(y|r_i)$ would be a one-hot-encoded vector [14,39], which can be defined as:

$$p(y|r_i) = \begin{cases} 1 & if y = y_i \\ 0 & otherwise \end{cases} \tag{1}$$

Based on the above objective, one can reduce the loss function as $L = \sum_{i=1}^{M \times N} H_i(p, q_\theta) = -\sum_{i=1}^{M \times N} \sum_{y=1}^{Y} p(y|r_i)\ log\ q_\theta(y|r_i) = -\sum_{i=1}^{M \times N} p(y_i|r_i)\ log\ q_\theta(y_i|r_i) = -\sum_{i=1}^{M \times N} log\ q_\theta(y_i|r_i)$. Minimizing L is equivalent to conduct maximum likelihood estimation over the training set. However, during optimisation, it is possible to minimize L to almost 0, if, and only if, all the instances in the dataset do not have conflicting labels (Conflicting labels means that there are two examples with the same features but their ground truths are different.) This is due to $q_\theta(y_i|r_i)$ being computed from soft-max as:

$$q_\theta(y_i|r_i) = \frac{exp(z_{y_i})}{\sum_{j=1}^{Y} exp(z_j)} \tag{2}$$

where z_i is the logit for candidate class i. The consequence of using one-hot-encoding is that $exp(z_{y_i})$ will be extremely large and $exp(z_j)$ where $j \neq y_i$ will be extremely small. Given a non-conflicting dataset, the ultimate model will classify every training instance correctly with the confidence of almost 1. This is certainly a signature of overfitting, and the overfitted model does not generalize well. Thus, this work used a regularization technique $\mu(y|r_i)$ (noise distribution) irrespective to traditional techniques proposed in literature [40–42] for deep models [43]. Thus, the new HSI ground truths (r_i, y_i) would be:

$$p'(y|r_i) = (1-\varepsilon)p(y|r_i) + \varepsilon\mu(y|r_i) \tag{3}$$

$$f(x) = \begin{cases} 1-\varepsilon+\varepsilon\mu(y|r_i) & if\ y = y_i \\ \varepsilon\mu(y|x_i) & otherwise \end{cases} \tag{4}$$

where $\varepsilon \in [0, 1]$ is a weight factor, and note that $\sum_{y=1}^{Y} p'(y|r_i) = 1$. These new ground truths have been used in loss function instead of one-hot-encoding [44]:

$$L' = -\sum_{i=1}^{M \times N} \sum_{y=1}^{Y} p'(y|r_i) \log q_\theta(y|r_i) \tag{5}$$

$$L' = -\sum_{i=1}^{M \times N} \sum_{y=1}^{Y} \big[(1-\varepsilon)p(y|r_i) + \varepsilon\mu(y|r_i)\big] \log q_\theta(y|r_i) \tag{6}$$

$$\begin{aligned} L' = \sum_{i=1}^{M \times N} \Bigg\{ (1-\varepsilon)\Big[-\sum_{y=1}^{Y} p(y|r_i) \log q_\theta(y|r_i)\Big] + \\ \varepsilon\Big[-\sum_{y=1}^{Y} \mu(y|x_i) \log q_\theta(y|r_i)\Big]\Bigg\} \end{aligned} \tag{7}$$

$$L' = \sum_{i=1}^{M \times N} \Big[(1-\varepsilon)H_i(p, q_\theta) + \varepsilon H_i(u, q_\theta)\Big] \tag{8}$$

where L' is the loss function, and p' is the estimated probabilities. It can be argued that, for each ground truth, the loss contribution is a mixture of entropy between predicted distribution ($H_i(p, q^\theta)$) and the one-hot-encoding, and the entropy between the predicted distribution ($H_i(\mu, q^\theta)$) and the noise distribution. While training, $H_i(p, q^\theta) = 0$ if the model learns to predict the distribution confidently; however, $H_i(\mu, q^\theta)$ will increase dramatically. To overcome this phenomenon, we used a regularizer $H_i(\mu, q^\theta)$ to prevent the model from predicting too confidently. In practice, $\mu(y|r)$ is a uniform distribution that does not depend on hyperspectral data. That is to say, $\mu(y|r) = \frac{1}{Y}$.

3. Experimental Settings and Results

The experiments have been conducted on three real HSI datasets, namely, Indian Pines (IP), Salinas full scene, and Pavia University (PU). These datasets are acquired by two different sensors. i.e., Reflective Optics System Imaging Spectrometer (ROSIS) and

Airborne Visible/Infrared Imaging Spectrometer (AVIRIS) [13]. The experimental results explained in this work have been obtained through Google Colab [45], an online platform to execute any Python environment even on Graphical Processing Unit (GPU), providing up to 358+ GB of cloud storage, and 25 GB of Random Access Memory (RAM).

In all the experiments, the initial size of the train/validation/test sets is set to 25%/25%/50% to validate the proposed model as well as several other state-of-the-art deep models. Five models have been used as baseline for the experiments: AlexNet, LeNet, 2D CNN, 3D CNN, and a Hybrid (3D/2D) CNN model. The details of the above-mentioned model are as follows.

1. The AlexNet model consists of five convolutional layers with 96, 256, 384, 384, 256 filters, while each layer has 7×7, 5×5, 3×3, 3×3, and 3×3 filter sizes. One pooling layer after the first convolutional layer. A flattened layer, dense layers with 4096 units. After each dense layer, a dropout layer has been used with 0.5%. Finally, an output layer has been used with the total number of classes to predict [46].
2. The LeNet model has two convolutional layers in which each layer has 32 and 64 filters with 5×5 and 3×3 filter sizes, respectively. One pooling layer after first convolutional layer, a flattened layer, dense layer with 100 units. Finally, an output layer has been used with the total number of classes to predict [47].
3. The 2D CNN model is composed of four convolutional layers in which each layer has 8, 16, 32, and 64 filters with 3×3 filter size. A flattened layer, two dense layers with 256 and 100 units, and, after each dense layer, a dropout layer has been used with 0.4%. Finally, an output layer has been used with the total number of classes to predict [32].
4. The 3D CNN is composed of four convolutional layers in which each layer has 8, 16, 32, and 64 filters with $3 \times 3 \times 7$, $3 \times 3 \times 5$, $3 \times 3 \times 3$, and $3 \times 3 \times 3$ filter sizes. A flattened layer, two dense layers with 256 and 128 units, and, after each dense layer, a dropout layer has been used with 0.4%. Finally, an output layer has been used with the total number of classes to predict [20].
5. The details of hybrid (3D/2D) convolutional layers and kernels are as follows: 3D conv layer $1 = 8 \times 5 \times 5 \times 7 \times 1$ i.e., $K_1^1 = 5, K_2^1 = 5$ and $K_3^1 = 7$. 3D conv layer $2 = 16 \times 5 \times 5 \times 5 \times 8$ i.e., $K_1^2 = 5, K_2^2 = 5$. $K_3^2 = 5$. 3D conv layer $3 = 32 \times 3 \times 3 \times 3 \times 16$ i.e., $K_1^3 = 3, K_2^3 = 3$ and $K_3^3 = 3$. 3D conv layer $4 = 64 \times 3 \times 3 \times 3 \times 32$ i.e., $K_1^3 = 3, K_2^3 = 3$ and $K_3^3 = 3$. 3D conv layer $5 = 128 \times 3 \times 3 \times 64$ i.e., $K_1^2 = 3$ and $K_2^2 = 3$. Three 3D convolutional layers are employed to increase the number of spectral-spatial feature maps, and one 2D convolutional layer is used to discriminate the spatial features within different spectral bands while preserving the spectral information.

Initially, the weights are randomized and then optimized using back-propagation with the Adam optimizer by using the loss function presented in Equation (8). Further details regarding the CNN architectures in terms of types of layers, dimensions of output feature maps and number of trainable parameters can be found in [13,20,32,46,47].

In order to validate the claims made in this manuscript, the following accuracy metrics have been assessed. They include: Kappa (κ is known as a statistical metric that considered the mutual information regarding a strong agreement among classification and ground-truth maps), average (AA represents the average class-wise classification performance), and overall (OA is computed as the number of correctly classified examples out of the total test examples). Such metrics are computed using the following equations:

$$\kappa = \frac{P_o - P_e}{1 - P_e} \tag{9}$$

where

$$P_o = \frac{TP + TN}{TP + FN + FP + TN}$$

$$P_e = \left(\frac{FN + TN}{TP + FN + FP + TN} \times \frac{FP + TN}{TP + FN + FP + TN} \right) + \frac{TP + FN}{TP + FN + FP + TN}$$

$$OA = \frac{1}{K} \sum_{i=1}^{K} TP_i \tag{10}$$

$$AA = \frac{TP + TN}{TP + TN + FN} \tag{11}$$

where TP and FP are true and false positive, TN and FN are true and false negative, respectively. For fair comparison purposes, the learning rate for all these models including hybrid models is set to 0.001, Relu as the activation function for all layers except the output layer on which Softmax is used, patch size is a set of 15, and, for all the experiments, the 15 most informative bands have been selected using principal component analysis to reduce the computational load. The convergence, accuracy, and loss of our proposed regularization technique with several CNN models for 50 epochs are presented in Figure 1. From loss and accuracy curves, one can conclude that the regularization has faster convergence.

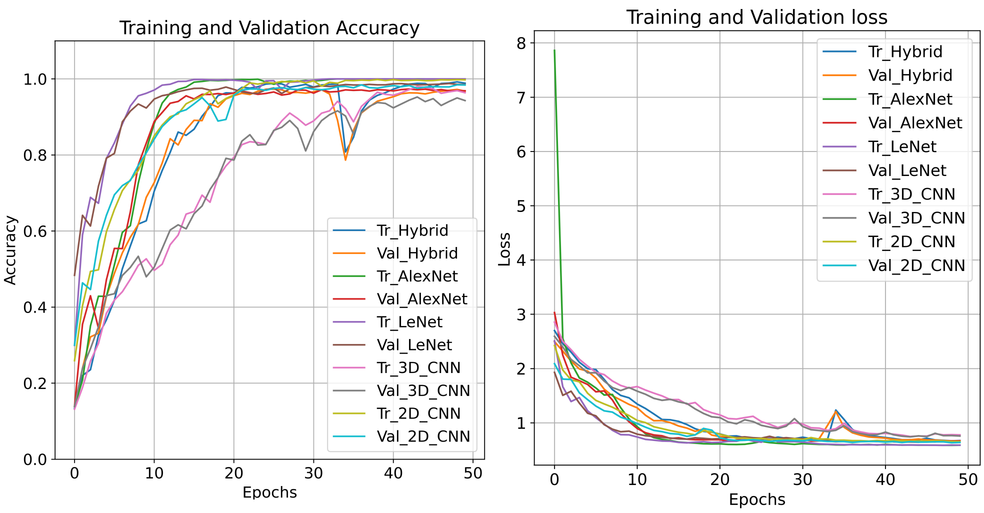

(**a**) Accuracy (**b**) Loss

Figure 1. Accuracy and loss for training and validation sets on Indian Pines for 50 epochs.

3.1. Indian Pines

The Indian Pines (IP) dataset is acquired using an AVIRIS sensor over the northwestern Indiana test site. IP data consist of 145×145 spatial dimensions and 224 spectral dimensions with a total of 16 classes in which all are not mutually exclusive. Some of the water absorption bands are removed, and the remaining 200 bands are used for the experimental process. These data consist of $2/3$ agriculture, $1/3$ forest, and other vegetation. Less than 5% of total coverage consists of crops that are in an early stage of growth. Building, low-density housing, two dual-lane highways, small roads, and a railway line are also a part of it. Further details about the experimental datasets can be found at [48]. Table 1 and Figure 2 present an in-depth comparative accuracy analysis on the IP dataset.

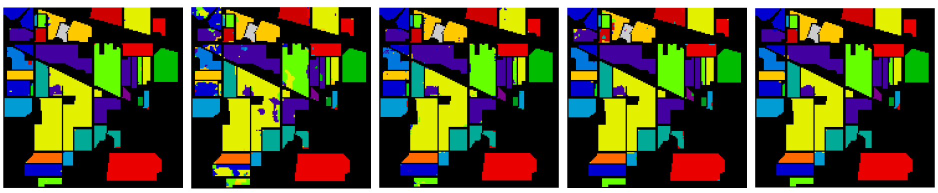

(**a**) 2D (**b**) 3D (**c**) A.Net (**d**) LeNet (**e**) Hybrid

Figure 2. Indian Pines: Classification accuracy: (**a**) 2D-CNN = 98.94%; (**b**) 3D CNN = 91.57%; (**c**) AlexNet = 97.65%; (**d**) LeNet = 98.14%; and (**e**) Hybrid = 99.29%.

Table 1. Indian Pines: Performance analysis of different state-of-the-art models trained using regularization technique.

Class	Train/Val/Test	2D	3D	AlexNet	LeNet	Hybrid
Alfalfa	11/12/23	100	91.3043	95.6521	82.6086	100
Corn-notill	357/357/714	98.3193	93.5574	97.3389	97.0588	98.8795
Corn-mintill	207/208/415	99.5180	66.7469	98.3132	99.5180	99.5180
Corn	59/59/118	94.0677	90.6779	93.2203	99.1525	100
Grass–pasture	121/121/242	98.3471	97.1074	96.2809	94.2148	96.2809
Grass–trees	182/183/365	98.9041	97.5342	98.3561	98.9041	99.7260
Grass-mowed	7/7/14	92.8571	92.8571	100	100	100
Hay-windrowed	119/120/239	100	100	100	100	100
Oats	5/5/10	70	0	100	70	100
Soybean-notill	243/243/486	98.5596	82.3045	93.6213	99.3827	97.9423
Soybean-mintill	614/614/1228	99.6742	92.4267	97.8013	99.9185	99.8371
Soybean-clean	148/149/297	97.6430	98.6531	96.9696	95.2861	99.6632
Wheat	51/51/102	99.0196	98.0392	100	99.0196	99.0196
Woods	316/317/633	99.8420	99.3680	99.5260	98.8941	99.8420
Buildings	96/97/193	99.4818	90.6735	100	91.1917	99.4818
Stone–steel	23/23/46	100	97.8260	100	93.4782	100
Training Time		55.6695	250.1662	919.5566	61.8763	248.5993
Test Time		1.4897	4.0402	5.6891	1.2752	3.9997
Overall Accuracy		98.9463	91.5707	97.6585	98.14634	99.2975
Average Accuracy		98.7980	86.8173	97.9425	94.9142	99.3869
Kappa (κ)		96.6396	90.3561	97.3312	97.8853	99.1990

3.2. Pavia University

The Pavia University (PU) dataset acquired using a Reflective Optics System Imaging Spectrometer (ROSIS) optical sensor over Pavia in northern Italy. The PU dataset is distinguished into nine different classes. PU consists of 610×610 spatial samples per spectral band and 103 spectral bands with a spatial resolution of 1.3 m. Further details about the experimental datasets can be found at [48]. Table 2 and Figure 3 present in-depth comparative accuracy analysis on the PU dataset.

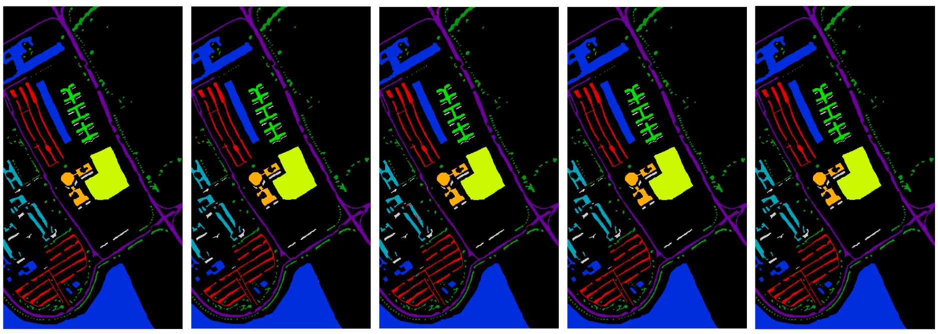

(**a**) 2D (**b**) 3D (**c**) A.Net (**d**) LeNet (**e**) Hybrid

Figure 3. Pavia University: Classification accuracy: (**a**) 2D-CNN = 99.9070%; (**b**) 3D CNN = 99.9256%; (**c**) AlexNet = 99.0768%; (**d**) LeNet = 99.9318%; and (**e**) Hybrid = 99.9628%.

Table 2. Pavia University: Performance analysis of different state-of-the-art models trained using regularization technique.

Class	Train/Val/Test	2D	3D	AlexNet	LeNet	Hybrid
Asphalt	1658/1658/3316	100	100	98.9143	100	100
Meadows	4662/4662/9324	100	99.9892	100	100	100
Gravel	524/525/1049	99.5233	99.3326	95.5195	99.4280	99.6186
Trees	766/766/1532	99.6736	100	98.8250	99.7389	100
Painted	336/337/673	100	100	100	100	100
Soil	1257/1257/2514	100	100	99.9602	100	100
Bitumen	332/333/665	100	100	99.6992	100	100
Bricks	920/921/1841	99.8913	99.8913	97.9359	100	99.8913
Shadows	237/237/74	99.3670	99.5780	98.5232	99.7890	100
Training Time		296.0174	1145.9233	4716.4900	308.6389	1143.4996
Test Time		5.7400	14.8634	24.1701	4.5054	15.5904
Overall Accuracy		99.9298	99.9438	99.3033	99.9485	99.9719
Average Accuracy		99.8283	99.8657	98.8197	99.8839	99.9455
Kappa (κ)		99.9070	99.9256	99.0768	99.9318	99.9628

3.3. Salinas

The Salinas (SA) dataset was acquired using an AVIRIS sensor over Salinas Valley, California and consists of 16 different classes—for instance, vineyard fields, vegetables, and bare soils. SA consists of 224 spectral bands in which each band is of size 512×217 with a 3.7 m spatial resolution. A few water absorption bands 108–112, 154–167, and 224 are removed before analysis. Further details about the experimental datasets can be found at [48]. Table 3 and Figure 4 present an in-depth comparative accuracy analysis on the Salinas dataset.

Table 3. Salinas: Performance analysis of different state-of-the-art models trained using regularization technique.

Class	Train/Val/Test	2D	3D	AlexNet	LeNet	Hybrid
Weeds 1	502/502/1005	100	100	100	100	100
Weeds 2	931/931/1863	100	100	100	100	100
Fallow	494/494/988	100	100	100	100	100
Fallow rough plow	348/348/698	100	100	100	100	100
Fallow smooth	669/669/1340	100	100	99.7012	100	100
Stubble	990/990/1980	100	100	100	100	100
Celery	894/894/1790	99.9441	100	100	100	100
Grapes untrained	2817/2818/5636	99.9822	100	99.9822	100	100
Soil vinyard develop	1550/1551/3102	100	100	100	100	100
Corn Weeds	819/820/1639	100	100	100	100	100
Lettuce 4wk	267/267/534	100	100	100	100	100
Lettuce 5wk	481/482/963	100	100	100	100	100
Lettuce 6wk	229/229/458	100	100	100	100	100
Lettuce 7wk	267/268/535	100	99.6261	100	100	100
Vinyard untrained	1817/1817/3634	99.8130	99.9174	99.1744	100	100
Vinyard trellis	451/452/904	100	100	100	100	100
Training Time	—	257.9992	1256.1199	4667.9047	288.3353	1267.9766
Test Time	—	7.3995	16.8058	27.8388	6.3860	19.2670
Overall Accuracy	—	99.9889	99.9815	99.8706	100.0	100.0
Average Accuracy	—	99.9837	99.9714	99.9286	100.0	100.0
Kappa (κ)	—	99.9876	99.9794	99.8559	100.0	100.0

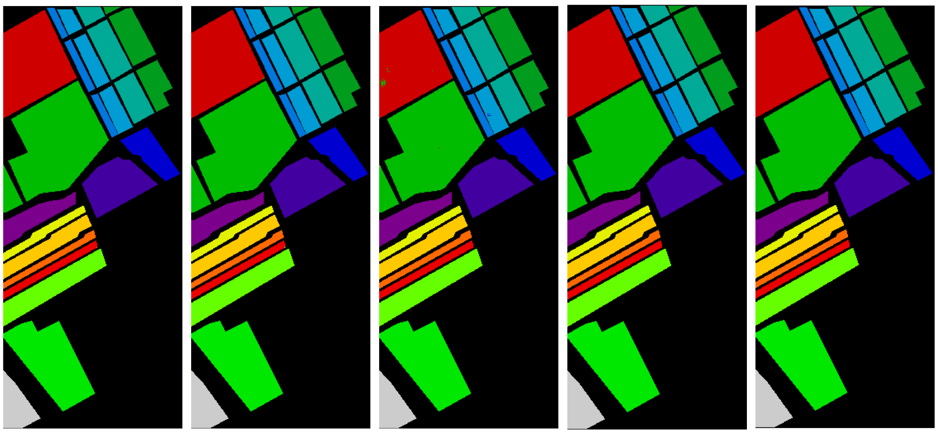

(**a**) 2D (**b**) 3D (**c**) A.Net (**d**) LeNet (**e**) Hybrid

Figure 4. Salinas: Classification accuracy: (**a**) 2D-CNN = 99.9876%; (**b**) 3D CNN = 99.9794%; (**c**) AlexNet = 99.8559%; (**d**) LeNet = 100.0%; and (**e**) Hybrid = 100.0%.

4. Comparison with State-of-the-Art Models

In all experimental results, the training, validation, and test sets are selected using a 5-fold cross-validation process with 25, 25, and 50% samples for training, validation, and test sets, respectively. The hybrid and all other competing models are trained using a 15×15 patch size because the classification performance strongly depends on the patch size, in which, if the patch size is too big, then the model may take pixels from various classes, whereas, if the patch size is too small, the model may decrease the inter-class diversity in samples. Hence, in both cases, the ultimate result will be in terms of a higher misclassification rate, leading to low generalization performance. Therefore, an appropriate patch size needs to be selected before the final experimental setup. The patch size selected in these experiments is based on the hit and trial method (i.e., provided the best accuracy).

The experimental results on benchmark HSI datasets are presented in Table 4. From these results, one can conclude that the proposed regularization process significantly improves the performance, in terms of accuracy, speed of convergence, and computational time. For comparison purposes, the framework, i.e., regularization for the Hybrid CNN model, is compared with various state-of-the-art works published in recent years. From the experimental results presented in Table 4, one can conclude that regularization with Hybrid CNN has obtained better results as compared to the state-of-the-art frameworks and, to some extent, outperformed with respect to the other models. The comparative models include a Support Vector Machine (SVM) with and without any grid optimization, Multi-layer Perceptron (MLP) having four fully connected layers with dropout, a 2D CNN model proposed by Sharma et al. [21], a semi-supervised CNN model proposed by Liu et al. [22], a 3D CNN model proposed by Hamida et al. [23], a hybrid CNN model proposed by Lee et al. [24] that consists of two 3D and eight 2D convolutional layers, a simple and compact 3D CNN model proposed by Chen et al. [25] that consists of three 3D convolutional layers, and a lightweight 3D CNN model proposed by Li et al. [26] that consists of two 3D convolutional layers and a fully connected layer. Li's work is different from traditional 3D CNN models as it uses fixed spatial-sized 3D convolutional layers with slight changes in spectral depth. Finally, multi-scale-3D-CNN [27], a fast and compact 3D-CNN (FC-3D-CNN) [20], and three different versions of Hybrid Depth-Separable Residual Network [28] were included.

All of the comparative models are being trained as per the settings mentioned in their respective papers except for the number of dimensions and patch size (i.e., 15 dimensions selected using PCA, and 15×15 path size). The experimental results listed in Table 4 show that the proposed framework has significantly improved results as compared to the other methods with fewer training samples.

Table 4. Experimental comparison with state-of-the-art models.

Methods	Salinas Full Scene			Indian Pines		
	OA	AA	Kappa	OA	AA	Kappa
MLP	79.79	67.37	77.40	87.57	89.07	85.80
SVM-Grid	67.39	45.89	62.80	87.93	88.02	86.20
SVM	92.95	94.60	92.11	85.30	79.03	83.10
FC-3D-CNN [20]	98.06	98.80	97.85	98.20	96.46	97.95
Xie et al. [21]	93.35	91.88	92.60	95.64	96.01	95.10
Liu et al. [22]	84.27	79.10	82.50	89.56	89.32	88.10
3D-CNN [23]	85.00	89.63	83.20	82.62	76.51	79.25
Lee et al. [24]	84.14	73.27	82.30	87.87	83.42	86.10
Chen et al. [25]	86.83	92.08	85.50	93.20	95.51	92.30
Li [26]	88.62	86.84	87.40	94.22	96.71	93.40
MS-3D-CNN [27]	94.69	94.03	94.10	91.87	92.21	90.80
Zhao et al. [28]	98.89	98.88	98.85	95.86	96.08	95.09
SyCNN-S [29]	97.44	98.46	97.20	95.90	97.84	95.30
SyCNN-D [29]	97.76	98.95	97.50	96.13	98.08	95.60
SyCNN-ATT [29]	98.92	99.35	98.80	97.31	98.43	96.90
Regularized AlexNet	99.87	99.92	99.85	97.65	97.94	97.33
Regularized LeNet	100.0	100.0	100.0	98.14	94.91	97.88
Regularized 2D	99.98	99.98	99.98	98.94	98.79	96.63
Regularized 3D	99.98	99.97	99.97	91.57	86.81	90.35
Regularized Hybrid	100.0	100.0	100.0	99.29	99.38	99.19

5. Conclusions

The paper proposed a regularized CNN feature hierarchy for HSIC, in which the loss contribution is considered as a mixture of entropy between a predicted distribution and the one-hot-encoding, and the entropy between the predicted and noise distribution. Several other regularization techniques (e.g., dropout, L1, L2, etc.) have also been used; however, these techniques, to some extent, lead to predicting the samples extremely confidently, which is not good from a generalization point of view. Therefore, this work proposed the use of an entropy-based regularization process to improve the generalization performance using soft labels. These soft labels are the weighted average of the hard labels and uniform distribution over entire ground truths. The entropy-based regularization process prevents CNN from becoming over-confident, while learning and predicting thus improves the model calibration and beam-search. Extensive experiments have confirmed that the proposed pipeline outperformed several state-of-the-art methods.

Author Contributions: Conceptualization, M.A.; Formal analysis, M.A. and S.D.; Funding acquisition, M.M.; Investigation, M.A. and S.D.; Methodology, M.A.; Project administration, M.M.; Supervision, M.M. and S.D.; Validation, M.A. and S.D.; Visualization, M.A. and M.M.; Writing—original draft, M.A., M.M., and S.D.; Writing—review and editing, M.A., M.M., and S.D. All authors have read and agreed to the published version of the manuscript.

Funding: This research received no external funding.

Institutional Review Board Statement: Not applicable.

Informed Consent Statement: Not applicable.

Data Availability Statement: Not applicable.

Conflicts of Interest: The authors declare no conflict of interest.

References

1. Alcolea, A.; Paoletti, M.E.; Haut, J.M.; Resano, J.; Plaza, A. Inference in Supervised Spectral Classifiers for On-Board Hyperspectral Imaging: An Overview. *Remote Sens.* **2020**, *12*, 534. [CrossRef]
2. Khabbazan, S.; Vermunt, P.; Steele-Dunne, S.; Ratering Arntz, L.; Marinetti, C.; van der Valk, D.; Iannini, L.; Molijn, R.; Westerdijk, K.; van der Sande, C. Crop Monitoring Using Sentinel-1 Data: A Case Study from The Netherlands. *Remote Sens.* **2019**, *11*, 1887. [CrossRef]
3. Oddi, L.; Cremonese, E.; Ascari, L.; Filippa, G.; Galvagno, M.; Serafino, D.; Cella, U.M.d. Using UAV Imagery to Detect and Map Woody Species Encroachment in a Subalpine Grassland: Advantages and Limits. *Remote Sens.* **2021**, *13*, 1239. [CrossRef]
4. Sun, X.; Wu, W.; Li, X.; Xu, X.; Li, J. Vegetation Abundance and Health Mapping Over Southwestern Antarctica Based on WorldView-2 Data and a Modified Spectral Mixture Analysis. *Remote Sens.* **2021**, *13*, 166. [CrossRef]
5. Moniruzzaman, M.; Thakur, P.K.; Kumar, P.; Ashraful Alam, M.; Garg, V.; Rousta, I.; Olafsson, H. Decadal Urban Land Use/Land Cover Changes and Its Impact on Surface Runoff Potential for the Dhaka City and Surroundings Using Remote Sensing. *Remote Sens.* **2021**, *13*, 83. [CrossRef]
6. Wang, B.; Shao, Q.; Song, D.; Li, Z.; Tang, Y.; Yang, C.; Wang, M. A Spectral-Spatial Features Integrated Network for Hyperspectral Detection of Marine Oil Spill. *Remote Sens.* **2021**, *13*, 1568. [CrossRef]
7. Menon, N.; George, G.; Ranith, R.; Sajin, V.; Murali, S.; Abdulaziz, A.; Brewin, R.J.W.; Sathyendranath, S. Citizen Science Tools Reveal Changes in Estuarine Water Quality Following Demolition of Buildings. *Remote Sens.* **2021**, *13*, 1683. [CrossRef]
8. Ayaz, H.; Ahmad, M.; Sohaib, A.; Yasir, M.N.; Zaidan, M.A.; Ali, M.; Khan, M.H.; Saleem, Z. Myoglobin-Based Classification of Minced Meat Using Hyperspectral Imaging. *Appl. Sci.* **2020**, *10*, 6862. [CrossRef]
9. Ayaz, H.; Ahmad, M.; Mazzara, M.; Sohaib, A. Hyperspectral Imaging for Minced Meat Classification Using Nonlinear Deep Features. *Appl. Sci.* **2020**, *10*, 6862. [CrossRef]
10. Khan, M.H.; Zainab, S.; Ahmad, M.; Sohaib, A.; Ayaz, H.; Mazzara, M. Hyperspectral Imaging for Color Adulteration Detection in Red Chili. *Appl. Sci.* **7783**, *10*, 5955. [CrossRef]
11. Khan, M.H.; Saleem, Z.; Ahmad, M.; Sohaib, A.; Ayaz, H.; Mazzara, M.; Raza, R.A. Hyperspectral imaging-based unsupervised adulterated red chili content transformation for classification: Identification of red chili adulterants. *Neural Comput. Appl.* **2021**. [CrossRef]
12. Saleem, Z.; Khan, M.H.; Ahmad, M.; Sohaib, A.; Ayaz, H.; Mazzara, M. Prediction of Microbial Spoilage and Shelf-Life of Bakery Products Through Hyperspectral Imaging. *IEEE Access* **2020**, *8*, 176986–176996. [CrossRef]
13. Ahmad, M.; Shabbir, S.; Raza, R.A.; Mazzara, M.; Distefano, S.; Khan, A.M. Hyperspectral Image Classification: Artifacts of Dimension Reduction on Hybrid CNN. *arXiv* **2021**, arXiv:2101.10532.
14. Wang, J.; Huang, R.; Guo, S.; Li, L.; Zhu, M.; Yang, S.; Jiao, L. NAS-Guided Lightweight Multiscale Attention Fusion Network for Hyperspectral Image Classification. *IEEE Trans. Geosci. Remote Sens.* **2021**, 1–14. [CrossRef]
15. Shabbir, S.; Ahmad, M. Hyperspectral Image Classification–Traditional to Deep Models: A Survey for Future Prospects. *arXiv* **2021**, arXiv:2101.06116.
16. Ahmad, M.; Khan, A.M.; Hussain, R.; Protasov, S.; Chow, F.; Khattak, A.M. Unsupervised geometrical feature learning from hyperspectral data. In Proceedings of the IEEE Symposium Series on Computational Intelligence (SSCI), Athens, Greece, 6–9 December 2016; IEEE Computational Intelligence Socity: New York, NY, USA, 2016; pp. 1–6.
17. Ahmad, M. Ground Truth Labeling and Samples Selection for Hyperspectral Image Classification. *Optik* **2021**, *230*, 166267. [CrossRef]
18. Ahmad, M.; Shabbir, S.; Oliva, D.; Mazzara, M.; Distefano, S. Spatial-prior generalized fuzziness extreme learning machine autoencoder-based active learning for hyperspectral image classification. *Optik* **2020**, *206*, 163712. [CrossRef]
19. Jia, S.; Jiang, S.; Lin, Z.; Li, N.; Xu, M.; Yu, S. A survey: Deep learning for hyperspectral image classification with few labeled samples. *Neurocomputing* **2021**, *448*, 179–204. [CrossRef]
20. Ahmad, M.; Khan, A.M.; Mazzara, M.; Distefano, S.; Ali, M.; Sarfraz, M.S. A Fast and Compact 3D CNN for Hyperspectral Image Classification. In *IEEE Geosci. Remote Sens. Lett.* **2020**, 1–5. [CrossRef]
21. Xie, Z.; Li, Y.; Niu, J.; Shi, L.; Wang, Z.; Lu, G. Hyperspectral face recognition based on sparse spectral attention deep neural networks. *Opt. Express* **2020**, *28*, 36286–36303. [CrossRef]
22. Liu, B.; Yu, X.; Zhang, P.; Tan, X.; Yu, A.; Xue, Z. A semi-supervised convolutional neural network for hyperspectral image classification. *Remote Sens. Lett.* **2017**, *8*, 839–848. [CrossRef]
23. Ben Hamida, A.; Benoit, A.; Lambert, P.; Ben Amar, C. 3D Deep Learning Approach for Remote Sensing Image Classification. *IEEE Trans. Geosci. Remote Sens.* **2018**, *56*, 4420–4434. [CrossRef]
24. Lee, H.; Kwon, H. Contextual deep CNN based hyperspectral classification. In Proceedings of the 2016 IEEE International Geoscience and Remote Sensing Symposium (IGARSS), Beijing, China, 10–15 July 2016; pp. 3322–3325. [CrossRef]
25. Chen, Y.; Jiang, H.; Li, C.; Jia, X.; Ghamisi, P. Deep Feature Extraction and Classification of Hyperspectral Images Based on Convolutional Neural Networks. *IEEE Trans. Geosci. Remote Sens.* **2016**, *54*, 6232–6251. [CrossRef]
26. Li, Y.; Zhang, H.; Shen, Q. Spectral–Spatial Classification of Hyperspectral Imagery with 3D Convolutional Neural Network. *Remote Sens.* **2017**, *9*, 67. [CrossRef]

27. He, M.; Li, B.; Chen, H. Multi-scale 3D deep convolutional neural network for hyperspectral image classification. In Proceedings of the 2017 IEEE International Conference on Image Processing (ICIP), Beijing, China, 17–20 September 2017; pp. 3904–3908.
28. Zhao, C.; Zhao, H.; Wang, G.; Chen, H. Hybrid Depth-Separable Residual Networks for Hyperspectral Image Classification. *Complexity* **2020**, *2020*, 4608647. [CrossRef]
29. Yang, X.; Zhang, X.; Ye, Y.; Lau, R.; Lu, S.; Li, X.; Huang, X. Synergistic 2D/3D Convolutional Neural Network for Hyperspectral Image Classification. *Remote Sens.* **2020**, *12*, 2033. [CrossRef]
30. Rumelhart, D.E.; Hinton, G.E.; Williams, R.J., Learning Representations by Back-Propagating Errors. In *Neurocomputing: Foundations of Research*; MIT Press: Cambridge, MA, USA, 1988; pp. 696–699.
31. Sha, H.; Al Hasan, M.; Mohler, G. Learning Network Event Sequences Using Long Short-Term Memory and Second-Order Statistic Loss. *Stat. Anal. Data Min.* **2021**, *14*, 61–73. [CrossRef]
32. Li, H.C.; Li, S.S.; Hu, W.S.; Feng, J.H.; Sun, W.W.; Du, Q. Recurrent Feedback Convolutional Neural Network for Hyperspectral Image Classification. *IEEE Geosci. Remote Sens. Lett.* **2021**, 1–5. [CrossRef]
33. Lei, R.; Zhang, C.; Du, S.; Wang, C.; Zhang, X.; Zheng, H.; Huang, J.; Yu, M. A non-local capsule neural network for hyperspectral remote sensing image classification. *Remote Sens. Lett.* **2021**, *12*, 40–49. [CrossRef]
34. Bi, H.; Santos-Rodriguez, R.; Flach, P. Polsar Image Classification via Robust Low-Rank Feature Extraction and Markov Random Field. In Proceedings of the IGARSS 2020—2020 IEEE International Geoscience and Remote Sensing Symposium, Waikoloa, HI, USA, 26 September–2 October 2020; pp. 708–711. [CrossRef]
35. Szegedy, C.; Vanhoucke, V.; Ioffe, S.; Shlens, J.; Wojna, Z. *Rethinking the Inception Architecture for Computer Vision*; In Proceedings of the 2016 IEEE Conference on Computer Vision and Pattern Recognition (CVPR), Las Vegas, NV, USA, 27–30 June 2016; doi:10.1109/CVPR.2016.308. [CrossRef]
36. Zhang, C.; Han, M. Multi-feature hyperspectral image classification with L2,1 norm constrained joint sparse representation. *Int. J. Remote Sens.* **2021**, *42*, 4789–4808. [CrossRef]
37. Real, E.; Aggarwal, A.; Huang, Y.; Le, Q.V. Regularized Evolution for Image Classifier Architecture Search. *Proc. AAAI Conf. Artif. Intell.* **2019**, *33*, 4780–4789. [CrossRef]
38. Zoph, B.; Vasudevan, V.; Shlens, J.; Le, Q.V. Learning Transferable Architectures for Scalable Image Recognition. *CoRR* **2017**, arXiv:1707.07012.
39. Yin, B.; Cui, B. Multi-feature extraction method based on Gaussian pyramid and weighted voting for hyperspectral image classification. In Proceedings of the 2021 IEEE International Conference on Consumer Electronics and Computer Engineering (ICCECE), Guangzhou, China, 15–17 January 2021; pp. 645–648. [CrossRef]
40. Zhou, H.; Song, L.; Chen, J.; Zhou, Y.; Wang, G.; Yuan, J.; Zhang, Q. Rethinking Soft Labels for Knowledge Distillation: A Bias-Variance Tradeoff Perspective. *arXiv* **2021**, arXiv:cs.LG/2102.00650.
41. Pham, H.H.; Le, T.T.; Tran, D.Q.; Ngo, D.T.; Nguyen, H.Q. Interpreting chest X-rays via CNNs that exploit hierarchical disease dependencies and uncertainty labels. *Neurocomputing* **2021**, *437*, 186–194. [CrossRef]
42. Song, M.; Zhao, Y.; Wang, S.; Han, M. Word Similarity Based Label Smoothing in Rnnlm Training for ASR. In Proceedings of the 2021 IEEE Spoken Language Technology Workshop (SLT), Shenzhen, China, 19–22 January 2021; pp. 280–285. [CrossRef]
43. Xie, F.; Gao, Q.; Jin, C.; Zhao, F. Hyperspectral Image Classification Based on Superpixel Pooling Convolutional Neural Network with Transfer Learning. *Remote Sens.* **2021**, *13*, 930. [CrossRef]
44. Yang, X.; Song, Z.; King, I.; Xu, Z. A Survey on Deep Semi-supervised Learning. *arXiv* **2021**, arXiv:cs.LG/2103.00550.
45. Carneiro, T.; Da Nóbrega, R.V.M.; Nepomuceno, T.; Bian, G.B.; De Albuquerque, V.H.C.; Reboucas Filho, P.P. Performance Analysis of Google Colaboratory as a Tool for Accelerating Deep Learning Applications. *IEEE Access* **2018**, *6*, 61677–61685. [CrossRef]
46. Mei, S.; Chen, X.; Zhang, Y.; Li, J.; Plaza, A. Accelerating Convolutional Neural Network-Based Hyperspectral Image Classification by Step Activation Quantization. *IEEE Trans. Geosci. Remote Sens.* **2021**, 1–12. [CrossRef]
47. Yuan, Y.; Wang, C.; Jiang, Z. Proxy-Based Deep Learning Framework for Spectral-Spatial Hyperspectral Image Classification: Efficient and Robust. *IEEE Trans. Geosci. Remote Sens.* **2021**, 1–15. [CrossRef]
48. Hyperspectral Datasets Description. 2021. Available online: http://www.ehu.eus/ccwintco/index.php/Hyperspectral_Remote_Sensing_Scenes (accessed on 1 April 2020).